Design, Modeling and Control of a 5-DoF Light-Weight Robot Arm for Aerial Manipulation

Carmine Dario Bellicoso, Luca Rosario Buonocore, Vincenzo Lippiello, and Bruno Siciliano

Abstract— The design, modeling and control of a 5 degrees-of-freedom light-weight robot manipulator is presented in this paper. The proposed robot arm, named *Prisma Ultra-Lightweight 5 ARm* (PUL5AR), is employed to execute manipulation tasks equipped on board of a vertical take-off and landing unmanned aerial vehicle. The arm is compact and light-weight. Its mechanics is designed such that it can fold on itself during landing manoeuvres. Moreover, the design is conceived to constrain the center of gravity of the arm as close as possible to vehicle base, thus reducing the total inertia and static unbalancing of the system. Experimental tests have been carried out in order to validate the dynamic model, the communication library, the developed electronics, and the control schemes implemented for the designed robot arm.

Index Terms— Aerial manipulation, light-weight robot arm, robot arm design.

Fig. 1.   ASCTEC PELICAN equipped with the PUL5AR.

I. INTRODUCTION

Unmanned Aerial Vehicles (UAVs) are attaining a growing importance both in civil and military applications. A number of tasks involving passive interaction with the environment, such as inspection, remote sensing or guarding [1], [2] have been investigated. By endowing a UAV with a robot arm taks such as manipulation and grasping [3] can be considered. However, the execution of such tasks poses a number of problems. The mechanical coupling between the two systems introduces stability issues due to the movement of the manipulator [4] and the interaction with the environment [5]. Moreover, the robot-arm plus vehicle dynamic models [6], [7], [8] need to be formulated and suitably estimated.

The extra degrees-of-freedom (DoFs) of the robot arm added to a UAV generate a redundant system, which can be exploited by assigning a number of subtasks [9], [10]. Pick-and-place tasks have been performed in [11], [12], where the gripper is made up by a task-specific structure with few DoFs. In [13] the grasping problem with a 3-DoF planar robot manipulator actuated by servomotors has been presented, while in [14] a UAV equipped with two robotic arms executes the task of closing a valve. A helicopter has been endowed with an industrial manipulator in [15], where by using visual measurement and an impedance control law the grasping of a bar has been executed.

C.D. Bellicoso is with ETH Zürich, Autonomous Systems Lab, LEE J 201, Leonhardstrasse 21, 8092 Zürich. Email: bellicoso@mavt.ethz.ch.

L.R. Buonocore, V. Lippiello, and B. Siciliano are with PRISMA Lab, Department of Electrical Engineering and Information Technology, University of Naples Federico II, via Claudio 21, 80125, Naples, Italy. Emails: lucarosario.buonocore@unina.it, lippiello@unina.it, siciliano@unina.it.

The authors are listed in alphabetical order.
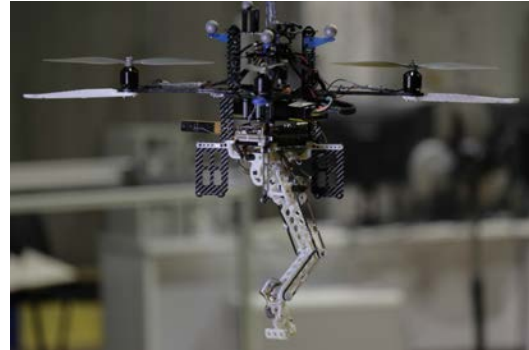
In this paper the issue of the kinematic coupling between the UAV attitude and the manipulator motion is addressed by the design of a differential joint at the base of the robotic arm. Moreover, with the relocation of motors at the base of the arm, the CoG remains close to the UAV body frame, hence the destabilizing effect on the UAV attitude due to the static torque generated by the misalignment of the CoGs is reduced [16]. Finally, the interaction capability with the environment is achieved by using motors and custom electronics to perform low-level torque control, thus allowing the implementation of impedance control laws [17].

In this work the constraints related to aerial robotics, such as payload and limited energy storage [18], have been considered too. The mechanical design of the arm is also inspired by the request to fold onto itself completely, in order to allow the UAV to take off and land without the need of particular structures. The target UAV used during the design is the ASCTEC PELICAN shown in Fig. 1, but the arm can be easily mounted on any kind of vertical take-off and landing (VToL) UAV with similar payload and computational board endowed with a USB. Experimental tests have been carried out by using the control and communication software specifically written for the arm.

II. MECHANICS

The mechanical design of the PUL5AR robot arm has been driven by the considered application, i.e. aerial manipulation with UAV endowed with a robotic arm. The target UAV is an ASCTEC PELICAN [19] with a payload of 650 g, but similar vehicles can be considered as well. The adopted specifications are as follows:

- Arm weight / payload: 250 g / 200 g.
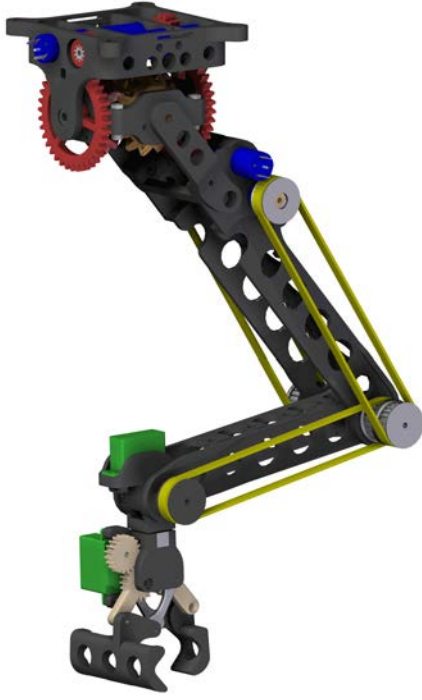- Arm maximum extension: 300 mm.

Fig. 2. PUL5AR robot arm (motors in blue, servos in green)

- Retain the possibility to execute VToL.
- Kinematics and dynamics decoupling.

The maximum weight constraint limits the mechanical design and the electronics. Notice that the weight/payload ratio is 1.25 unlike the case of typical industrial robots (roughly 20). By using a honeycomb structure, a reduction of the total weight can be achieved (see Fig. 2). However, this choice affects the elasticity of the mechanical structure, hence FEM analysis has been carried out, as shown in Fig. 3. The mechanical parts have been built with a 3D printer that uses a material composed by acrylic monomer.
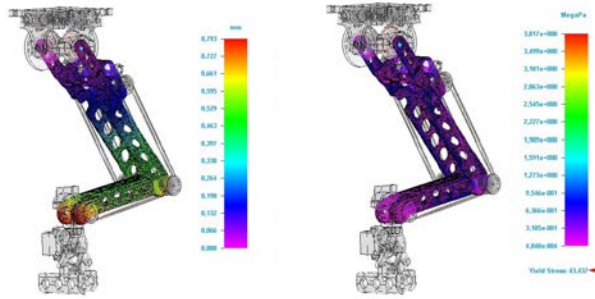

Fig. 3. FEM analysis: displacement (left) and stress (right) due to an applied payload of 160 g.

Aerial manipulation tasks suggests mounting the arm under the UAV. Therefore, the mechanical structure was designed such that the arm could fold onto itself completely to reduce the occupied space during the take-off and landing phases (see Fig. 4).
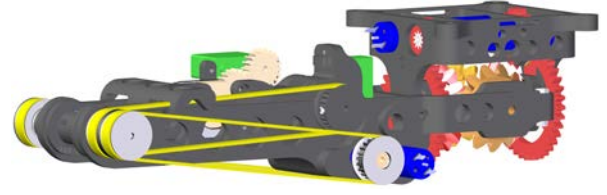

Fig. 4. CAD rendering of the PUL5AR robot arm in fold configuration.

Six actuators are used in the arm: 4 DC motors for the first joints, and 2 digital servomotors for the last joint and the gripper. The first two DC motors are included into the base of the arm, while the last two are positioned at the beginning of the second joint. For the latter, a MXL timing belts 4.8 mm wide is employed for the motion transmission. The first two joints have been designed as differential joints (see Fig. 2) in order to allow the active compensation of the UAV roll-pitch motions on the manipulator's end-effector position. Moreover, positioning of the first two motors inside the base reduces the arm's inertia. Further, the adoption of timing belts has allowed relocating the other two motors at the base of the first link. The drawback is the backlash due to the differential and transmission mechanisms.
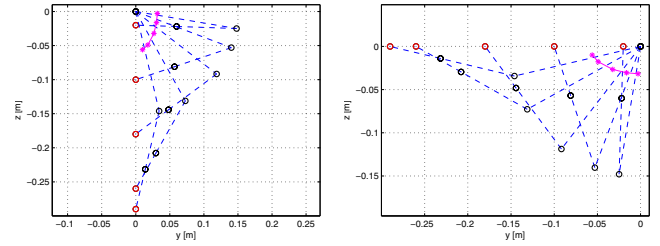

Fig. 5. Variation of the position of the arm's CoG (magenta) with respect to different joint configurations corresponding to the gripper center (red) moving along the vertical (left) and horizontal (right) axes.
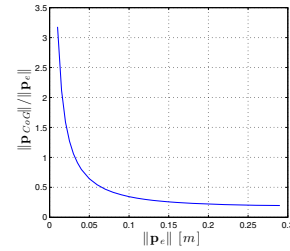

Fig. 6. Diagram of the ratio of the distances of the robot's CoG p_{CoG}^b and of the gripper position p_e^b, from the robot base, with respect to $\|p_e^b\|$.

Figure 5 shows the position of the arm CoG $p_{CoG}(q)$ for several joint configurations q that correspond to the gripper center $p_e(q)$ moving along the vertical and horizontal axes. Figure 6 shows how the CoG moves away from the base slowly with respect to the corresponding distance of the gripper. This behavior is particularly advantageous because it allows moving the arm throughout the workspace by introducing a limited static disturbance on the UAV body.

In our case study, the geometrical dimensions of the arm have been adapted to mounted it under an ASCTEC PELICAN. The maximum reachable distance and payload are a design tradeoff constrained by the electrical and mechanical power of the actuators and gearboxes, respectively. In view of the considered specifications, MAXON RE 10 motors have been chosen. They have a weight/power ratio of 12 g/W, with a maximum continuous torque of 1.2 Nm joint side. The small size suggests the use of two digital servomotors to actuate the last joint and the gripper (see Fig. 2).

III. MODELING

The PUL5AR robot arm was modeled following the formalism given in [6]. Kinematic modeling is based on the Denavit-Hartenberg (DH) convention and the existing mechanical coupling has been considered. The dynamic model is evaluated using the Euler-Lagrange energy formulation. Its parameters have been estimated with the CAD model and validated experimentally.
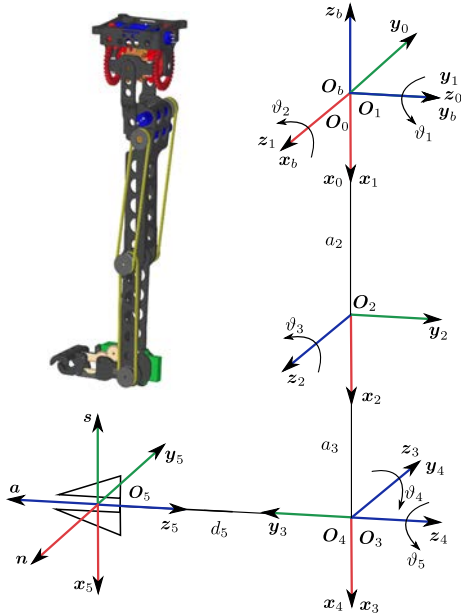

Fig. 7. The joints reference frames chosen following the Denavit-Hartenberg convention. The robot is shown in $\boldsymbol{q} = \boldsymbol{0}$ configuration.

A. Reference frames and kinematic coupling

The evaluated DH parameters and frames are described in Table I and in Fig. 7, respectively. Since all the joints in the

Link	a_i	α_i	d_i	ϑ_i
1	0	$\pi/2$	0	ϑ_1
2	150	0	0	ϑ_2
3	88	-π	0	ϑ_3
4	0	$\pi/2$	0	ϑ_4
5	0	0	-60	ϑ_5

TABLE I

DENAVIT-HARTENBERG PARAMETERS (LENGTHS ARE IN mm).

PUL5AR robot are revolute, the position vector in the joint

space is given by $\boldsymbol{q} = \begin{bmatrix} q_1 & \cdots & q_5 \end{bmatrix}^T = \begin{bmatrix} \vartheta_1 & \cdots & \vartheta_5 \end{bmatrix}^T$. The kinematic coupling due to the differential joint and to the designed motion transmission mechanisms can be represented in compact form as follows:

$$\boldsymbol{q}_m = \begin{bmatrix} k_r k_d & k_r k_d & 0 & 0 & 0 \\ -k_r k_d & k_r k_d & 0 & 0 & 0 \\ 0 & 0 & k_r & 0 & 0 \\ 0 & 0 & -k_r & k_r & 0 \\ 0 & 0 & 0 & 0 & 1 \end{bmatrix} \boldsymbol{q} = \boldsymbol{H}\boldsymbol{q}, \quad (1)$$

where $\boldsymbol{q}_m \in \mathbb{R}^5$ represents the motor position, while $k_r = 256$ and $k_d = 3$ are the chosen gear and differential ratio, respectively, and the matrix $\boldsymbol{H}$ projects the joint space to the motor space. It can be easily shown that $\det(\boldsymbol{H}) = 2k_d^2 k_r^4 > 0$, hence (1) can be inverted yielding:

$$\boldsymbol{q} = \boldsymbol{H}^{-1}\boldsymbol{q}_m. \quad (2)$$

Equations (1) and (2) show how q_{m1} and q_{m2} actuate joints q_1 and q_2, q_{m3} and q_{m4} actuate joints q_3 and q_4, while q_5 is independent. Finally, differentiating (1) yields[1]:

$$\dot{\boldsymbol{q}}_m = \boldsymbol{H}\dot{\boldsymbol{q}}. \quad (3)$$

Assuming an ideal model for the gear ratios, the motor torques $\boldsymbol{\tau}_m$ and the joint torques $\boldsymbol{\tau}$ are related as follows:

$$\boldsymbol{\tau}^T\dot{\boldsymbol{q}} = \boldsymbol{\tau}_m^T\dot{\boldsymbol{q}}_m = \boldsymbol{\tau}_m^T\boldsymbol{H}\dot{\boldsymbol{q}} \quad \forall\dot{\boldsymbol{q}} \quad \Rightarrow \quad \boldsymbol{\tau}_m = \boldsymbol{H}^{-T}\boldsymbol{\tau}. \quad (4)$$

B. Direct and differential kinematics

The arm direct kinematics is represented by the following homogeneous transformation matrix:

$$\boldsymbol{T}_e^b(\boldsymbol{q}) = \begin{bmatrix} \boldsymbol{R}_e^b(\boldsymbol{q}) & \boldsymbol{p}_e^b(\boldsymbol{q}) \\ \boldsymbol{0} & 1 \end{bmatrix}, \quad (5)$$

where $\boldsymbol{p}_e^b(\boldsymbol{q})$ and $\boldsymbol{R}_e^b(\boldsymbol{q})$ represent the position vector and rotation matrix of the end effector with respect to the base frame, respectively. The differential kinematics is represented by the so called *geometric Jacobian* matrix (see [6]), i.e.

$$\boldsymbol{v}_e = \begin{bmatrix} \dot{\boldsymbol{p}}_e(\boldsymbol{q}) \\ \boldsymbol{\omega}_e(\boldsymbol{q}) \end{bmatrix} = \begin{bmatrix} \boldsymbol{J}_P(\boldsymbol{q}) \\ \boldsymbol{J}_O(\boldsymbol{q}) \end{bmatrix} \dot{\boldsymbol{q}} = \boldsymbol{J}(\boldsymbol{q})\dot{\boldsymbol{q}}. \quad (6)$$

The plain expression of these terms is omitted for brevity.

Since five DoFs are present in the system, the corresponding geometric Jacobian is a (6×5) matrix. In fact, the orientation of the gripper cannot be freely specified if its positions has already been assigned. This also corresponds to choosing an *operational space* with a 5 or lower dimension. A possible choice can be:

$$\boldsymbol{\theta}(\boldsymbol{q}) = \begin{bmatrix} \phi(\boldsymbol{q}) \\ \psi(\boldsymbol{q}) \end{bmatrix} = \begin{bmatrix} q_2 + q_3 - q_4 \\ q_5 \end{bmatrix}. \quad (7)$$

This choice is natural because the mechanical structure of the arm lies entirely on a plane if the position $\boldsymbol{p}_e^b(q)$ has been specified. Therefore, the rotation of the end-effector can be

[1]Due to the kinematic coupling, the transformation between $\dot{\boldsymbol{q}}$ and $\dot{\boldsymbol{q}}_m$ is not actually linear, but it should be modified to take into account the saturation on the maximum velocity of each motor, which does not linearly map onto velocity saturations on the joints, but makes $\boldsymbol{H}$ configuration dependent.

naturally assigned along the gripper approaching axis and $z_1^b(q)$. With this choice the direct kinematics becomes:

$$x_e(q) = \begin{bmatrix} p_e(q) \\ \theta(q) \end{bmatrix} = k(q) \qquad (8)$$

Differentiating (8) with respect to time yields:

$$\dot{x}_e(q) = \frac{\partial k(q)}{\partial q} \dot{q} = \begin{bmatrix} J_p(q) \\ J_\theta(q) \end{bmatrix} \dot{q} = J_A(q)\dot{q}, \qquad (9)$$

where $J_A(q)$ is the so called *analytical Jacobian* matrix.

C. Kinematic singularities

By inverting (6), the end-effector velocity is projected onto the joint space by the generalized inverse of matrix $J(q)$. Whenever $\mathrm{rank}\,[J(q)] < 5$ the equation in (6) becomes linearly dependent and the corresponding q are named *singular configurations*. Solution $\dot{q}$ can be evaluated only if $v_e \in \mathcal{R}(J)$, i.e. if the motion is locally physically executable. If instead it is $v_e \notin \mathcal{R}(J)$, equation (6) has no solution and the motion is not kinematically executable. The analysis of the singular configurations is of particular importance when closed-loop inverse kinematics algorithms are employed.

The computation of the determinant of $J_A(q)$ yields:

$$\begin{aligned}
\det(J_A(q)) = \frac{1}{2}(a_2 a_3 (a_2 \sin(\vartheta_2 + \vartheta_3) \\
+ d_5 \cos(\vartheta_2 + 2\vartheta_3 - \vartheta_4) - a_3 \sin(\vartheta_2) \\
- d_5 \cos(\vartheta_2 - \vartheta_4) - a_2 \sin(\vartheta_2 - \vartheta_3) \\
+ a_3 \sin(\vartheta_2 + 2\vartheta_3))),
\end{aligned} \qquad (10)$$

and one can observe that $det(J_A(q))$ does not depend on ϑ_1, nor on ϑ_5. It can be shown that:

$$\vartheta_3 = 0 \implies \det(J_A(q)) = 0 \;\; \forall \vartheta_1, \vartheta_2, \vartheta_4, \vartheta_5. \qquad (11)$$

D. Dynamic model and validation

The dynamic model of the PUL5AR robot arm has been evaluated using the Lagrange method [6]. The compact form of the dynamic model can be conveniently written as:

$$\begin{aligned}
B(q)\ddot{q} + (C(q,\dot{q}) + F_v)\dot{q} + F_s\mathrm{sgn}(\dot{q}) + g(q) \\
= H^T \tau_m - J^T(q)h_e
\end{aligned} \qquad (12)$$

where $B(q)$ is symmetric and positive definite inertia matrix, $C(q,\dot{q})$ represents the centrifugal and Coriolis effect, $g(q)$ represents the gravity term, F_v and F_s are diagonal and positive definite matrices representing viscous and static friction effects, and h_e is the vector of the forces exerted by the end effector on the environment.

The dynamic model is a function of a set of dynamic parameters. For each link i one can define the mass m_{ℓ_i}, the inertia tensor $I_{\ell_i} \in \mathbb{R}^{3\times3}$, and the CoG p_{ℓ_i}. In order to simplify the model, the mass of the motors and their inertia tensor are included in the link related parameters. In particular, masses m_{ℓ_5} and m_{ℓ_4} include the masses of the servomotors m_{m_6} and m_{m_5}, respectively, where m_{m_6} is the mass of the gripper actuator. The parameter m_{ℓ_2} takes into

account masses m_{m_3} and m_{m_4}. Notice that m_{m_1} and m_{m_2} do not add contributions to the motion equations, since the first two motors are mounted on the base, i.e. they are added to the mass of the UAV base.

The inertial parameters have been estimated through the CAD model and the motor data-sheets of the motors and are described in Table II. Notice that, p_{ℓ_i} and I_{ℓ_i} are constant with respect to the ith link reference frame.

Link	m	p_{CoG_x}	p_{CoG_y}	p_{CoG_z}
1	28.654	0.00	-0.02	0.87
2	73.16	-86.37	10.4	0.23
3	11.815	-41.44	1.71	-1.42
4	7.968	-3.93	0.11	8.15
5	14.52	-6.88	-3.86	28.73

Link	I_{xx}	I_{xy}	I_{xz}	I_{yy}	I_{yz}	I_{zz}
1	96.20	0.01	0.0	49.48	0	66.08
2	219.96	-106.84	26.85	1298.95	-3.18	1147.79
3	11.23	-0.8	-11.0	161.04	0.32	156.05
4	7.24	0.04	-1.27	9.32	-0.08	3.76
5	37.23	2.46	0.68	44.65	-3.82	25.61

TABLE II

DYNAMIC PARAMETERS OF THE PUL5AS ROBOT ARM. TOP: MASS [g] AND COG [mm]; BOTTOM: INERTIA TENSOR $[10^{-7}\mathrm{kg}\cdot\mathrm{m}^2]$. ALL QUANTITIES ARE EXPRESSED IN THE CORRESPONDING LINK FRAME.

The dynamic parameters estimated by the CAD model have been experimentally validated by comparing the measured torques acting on the motors with those predicted by the dynamic model as follows:

- generate a trajectory in joint space with the developed planner (see Fig. 9 and the corresponding Cartesian trajectory in Fig. 8);
- measure position, velocity and current from each motor.

In this work, an indirect torque measurement τ can be achieved from the currents using:

$$\tau = H^T \tau_m = H^T k_t i_a. \qquad (13)$$

Notice that the evaluation of the predicted torques $\bar{\tau}$ also needs the accelerations $\ddot{q}$, that can be obtained by filtering and differentiating the velocities $\dot{q}$.
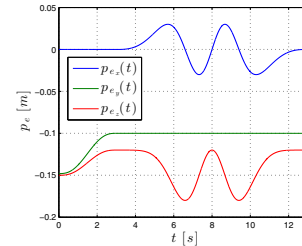

Fig. 8. Time history of the reference trajectory in the Cartesian space employed for the dynamic model validation.

Figure 9 shows that, by using an accurate 3D printer and by estimating friction with an identification process, the estimated parameters are sufficiently precise.
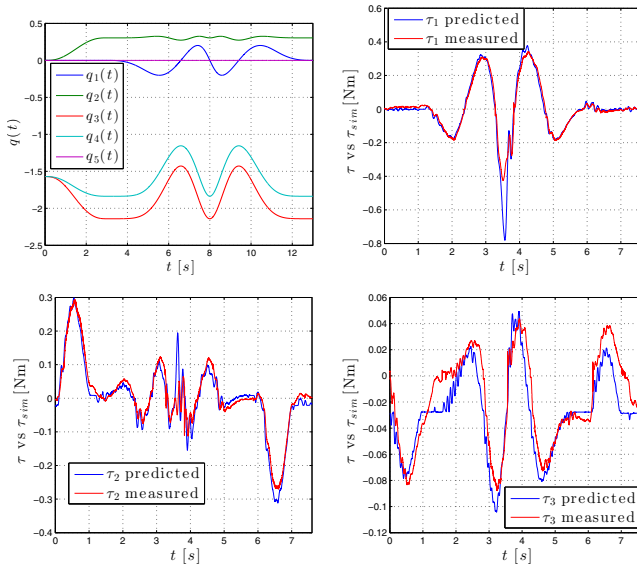
Fig. 9. Time history of the joint trajectories employed for the dynamic model validation (top-left), and dynamic model validation: comparison between the predicted (blue) and the measured (red) values of τ_1 (top-right), τ_2 (bottom-left), and τ_3 (bottom-right).

Fig. 10. Hardware architecture of the low-level control system.

Fig. 11. Power drive and acquisition modules (BOARD # in Fig. 10).

IV. CUSTOM ELECTRONICS

The presence of a centralized control node generates some communication issues with the single motor node. The problem gains importance in consideration of the target feedback loops rate, nominally 4 kHz for the current loop and 1 kHz for the velocity and position loop, which are required for the implementation of a high-level interaction control law.

For each DC motor the acquisition of the position and current is required. An MBED LPC1768 [20] microcontroller (μC) has been employed as an interface between the communication layer and the direct access to the low-level electronic components (motor drives, sensors, etc.). A serial peripheral interface (SPI) bus, with a high data rate and a limited number of connections, is employed to drive data and acquire measurements close to the sources (i.e. reducing electrical noise). Moreover, with dedicated measurement acquisition chips the μC computational load is reduced, e.g. hardware interrupt due to the encoders. In order to further reduce the μC computational load, each servomotor is interfaced by means of a PCA9685, that generates the PWM control signals and communicates by using the SPI bus. Hence, the μC mainly implements the communication protocol through the USB bus, reads the data on the SPI, and closes current, velocity and position control loops. The overall architecture is shown in Fig. 10.

A 40 kHz PWM signal generated by the μC is used to drive the DC motors through a Texas Instruments DRV8801 full-bridge (2.8 A peak current). These drives also allow the measurement of the motor current, which is amplified, filtered and then acquired by an ADC MCP3202 (100 ksample/s) and sent on the SPI bus to the μC. The encoder pulses are counted by a LS7366 dedicated chip, which is a 32-bit counter working at 40 MHz. Figure 11 shows the block
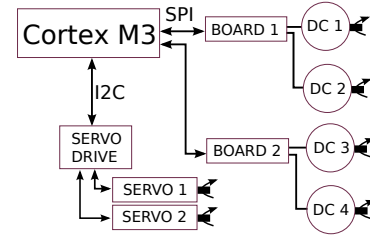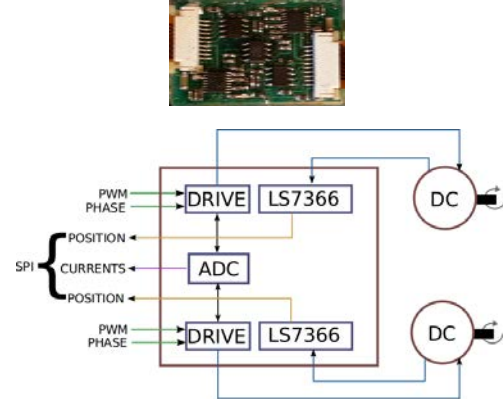
scheme of the power drive and acquisition modules.

Mechanical switches connected to the μC have been used as joint limits detectors. Using these sensors an automatic *homing* procedure has been implemented, allowing the arm to find the folded configuration and kinematically calibrate.

V. COMMUNICATION PROTOCOL

A communication protocol has been designed to command the robot with a host computer endowed of a USB. The USB bus has been chosen for the high-speed data rate and for its wide diffusion on high-level elaboration boards.

The protocol allows specifying a command, an identifier, and a data field. The host can request a reading, send a reference value, and set the μC and connected devices configurations. In this operational mode, the host synchronizes the μC, which waits for a new request. In a different operational mode, the μC periodically triggers the host by sending the sensor measurement, and the host replies with the references for the motors. Dynamically sized packets have been implemented in order to optimize bandwidth consumption. Notice that the data exchange between the μC and the host is very slow with respect to the other operations.

Each data packet (see Fig. 12) has a 2-bytes header and a variable length data field. The header is made up by a command byte, that specifies the packet type, and an identification byte, that specifies the target device (DC motor, servomotor, feedback loop, etc.).

The round trip time (RTT) —the time delay between the start of a request packet and the end of the reply— of the average data packet is considered to validate the proposed solution. In Fig. 13 the RTT for the motors position

C	I	DATA			
0x64	0x93	0xdb	0x0f	0xc9	0x3f

Fig. 12. Structure of a generic data packet: command (C), identification (I), and data field. Each square represents a byte.
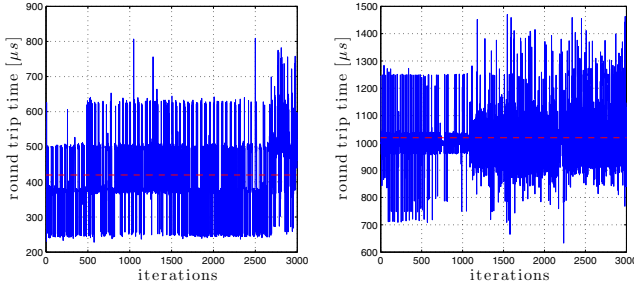

Fig. 13. RTT measured for the request of all the motor positions (on the left, mean value is about 420 μs) and for sending and receiving a 50 byte packet (on the right, mean value is about 420 μs).

request and for sending and receiving a 50 byte packet are shown. The measured performances show that a control loop of more than 500 Hz can be achieved with a reasonable safety margin. The small oscillations of the transmission rate partially depend on the adoption of the USB bulk transmissions protocol, which guarantees integrity of the data packet but not a bounded transmission delay. To further improve the stability of the communication rate, work is in progress to switch to the isochronous transmission protocol.

An SDK library has been designed for the host computer, that hides the details of the communication implementation.

VI. Independent joint control

The low-level motor control is a classical cascade position-velocity-current loops. When the position control is active, both velocity and current feedforward references can be sent. By opening the outer control loops, both a velocity (with current feedforward) and a current control can be achieved.
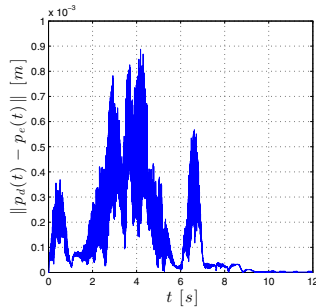

Fig. 14. Norm of tracking error with the trajectory shown in Fig. 8.

Figure 14 shows that the tracking error corresponding to the trajectory of Fig. 8 is less than 1 mm during transient (0.3% of the arm length) and goes to zero at steady state.

VII. Conclusions

The design of a lightweight robotic arm for aerial manipulation has been presented. Mechanical and electronics design

were constrained by energy and payload limitations with the goal of maximizing the payload and the displacement of the CoG. Both the kinematic and the dynamic model, as well as the communication and control performances were estimated and validated through experimental tests.

References

[1] C. Doyle, J. Bird, T. Isom, C. Johnson, J. Kallman, J. Simpson, R. King, J. Abbott, and M. Minor, "Avian-inspired passive perching mechanism for robotic rotorcraft," in *IEEE/RSJ International Conference on Intelligent Robots and Systems*, 2011, pp. 4975–4980.

[2] C. Doyle, J. Bird, T. Isom, J. Kallman, D. Bareiss, D. Dunlop, R. King, J. Abbott, and M. Minor, "An avian-inspired passive mechanism for quadrotor perching," *IEEE/ASME Transactions on Mechatronics*, vol. 18, no. 2, pp. 506–517, 2013.

[3] P. Pounds and A. Dollar, "Aerial grasping from a helicopter UAV platform," in *Experimental Robotics*, ser. Springer Tracts in Advanced Robotics, O. Khatib, V. Kumar, and G. Sukhatme, Eds. Springer Berlin Heidelberg, 2014, vol. 79, pp. 269–283.

[4] F. Ruggiero, J. Cacace, H. Sadeghian, and V. Lippiello, "Impedance control of VToL UAVs with a momentum-based external generalized forces estimator," in *IEEE International Conference on Robotics and Automation*, 2014.

[5] P. Pounds and A. Dollar, "UAV rotorcraft in compliant contact: stability analysis and simulation," *in IEEE/RSJ International Conference on Intelligent Robots and Systems*, pp. 2660–2667, 2011.

[6] B. Siciliano, L. Sciavicco, L. Villani, and G. Oriolo, *Robotics: Modeling, Planning and Control*. Springer, 2009.

[7] B. Siciliano and O. Khatib, *Springer Handbook of Robotics*. Springer, 2009.

[8] K. Nonami, F. Kendoul, S. Suzuki, W. Wang, and D. Nakazawa, *Autonomous Flying Robots*. Springer, 2010.

[9] V. Lippiello and F. Ruggiero, "Exploiting redundancy in cartesian impedance control of UAVs equipped with a robotic arm," in *IEEE/RSJ International Conference on Intelligent Robots and Systems*, 2012, pp. 3768–3773.

[10] G. Arleo, F. Caccavale, G. Muscio, and F. Pierri, "Control of quadrotor aerial vehicles equipped with a robotic arm," in *21st Mediterranean Conference on Control Automation*, 2013, pp. 1174–1180.

[11] F. Forte, R. Naldi, A. Macchelli, and L. Marconi, "Impedance control of an aerial manipulator," in *American Control Conference*, 2012, pp. 3839–3844.

[12] Q. Lindsey, D. Mellinger, and V. Kumar, "Construction of cubic structures with quadrotor reams," in *Proceedings of Robotics: Science and Systems*, 2011.

[13] A. E. Jimenez-Cano, J. Martin, G. Heredia, A. Ollero, and R. Cano, "Control of an aerial robot with multi-link arm for assembly tasks." in *IEEE International Conference on Robotics and Automation*, 2013, pp. 4916–4921.

[14] M. Orsag, C. Korpela, S. Bogdan, and P. Oh, "Valve turning using a dual-arm aerial manipulator," in *International Conference on Unmanned Aircraft Systems*, 2014, pp. 836–841.

[15] F. Huber, K. Kondak, K. Krieger, D. Sommer, M. Schwarzbach, M. Laiacker, I. Kossyk, S. Parusel, S. Haddadin, and A. Albu-Schaffer, "First analysis and experiments in aerial manipulation using fully actuated redundant robot arm," in *IEEE/RSJ International Conference on Intelligent Robots and Systems*, 2013, pp. 3452–3457.

[16] P. E. Pounds, D. R. Bersak, and A. M. Dollar, "Stability of small-scale UAV helicopters and quadrotors with added payload mass under PID control," *Autonomous Robots*, vol. 33, no. 1-2, pp. 129–142, 2012.

[17] V. Lippiello and F. Ruggiero, "Cartesian impedance control of a UAV with a robotic arm," in *10th International IFAC Symposium on Robot Control*, 2012.

[18] R. C. Julian, C. J. Rose, H. Hu, and R. S. Fearing, "Cooperative control and modeling for narrow passage traversal with an ornithopter MAV and lightweight ground station," in *International Conference on Autonomous Agents and Multi-agent Systems*, 2013, pp. 103–110.

[19] Ascending technologies, gmbh. [Online]. Available: http://www.asctec.de/

[20] Nxp mbed: development platform for devices. [Online]. Available: http://www.mbed.org/